Quantifying noise effects in optical measures of excited state transport

Joseph J. Thiebes[1] and Erik M. Grumstrup[1,2,a)]

[1]Department of Chemistry & Biochemistry, Montana State University, Bozeman, Montana 59717, United States

[2]Montana Materials Science Program, Montana State University, Bozeman, Montana 59717, United States

ABSTRACT

Time-resolved microscopy is a widely used approach for imaging and quantifying charge and energy transport in functional materials. While it is generally recognized that resolving small diffusion lengths is limited by measurement noise, the impacts of noise have not been systematically assessed or quantified. This manuscript reports modeling efforts to elucidate the impact of noise on optical probes of transport. Excited state population distributions, modeled as Gaussians with additive white noise typical of experimental conditions, are subject to decay and diffusive evolution. Using a conventional composite least-squares fitting algorithm, the resulting diffusion constant estimates are compared with the model input parameter. The results show that heteroscedasticity (*i.e.*, time-varying noise levels), insufficient spatial and/or temporal resolution, and small diffusion length relative to the magnitude of noise lead to a surprising degree of imprecision under moderate experimental parameters. Moreover, the compounding influence of low initial contrast and small diffusion length leads to systematic over-estimation of diffusion coefficients. Each of these issues is quantitatively analyzed herein and experimental approaches to mitigate them are proposed. General guidelines for experimentalists to rapidly assess measurement precision are provided,

[a)] Author to whom correspondence should be addressed. Electronic mail: erik.grumstrup@montana.edu

as is an open-source tool for customizable evaluation of noise effects on time-resolved microscopy transport measurements.

I. INTRODUCTION

Time-resolved optical microscopy has recently gained prominence as an effective tool to study excited state transport in materials relevant to photovoltaic, photocatalytic, lighting, and other optoelectronic materials.[1-5] For such measurements, a short laser pulse is focused with a high numerical aperture lens, producing a localized population of excited states. The spatial and temporal evolution of the photogenerated excited state population is then probed with a spatially offset second laser pulse (in the case of pump-probe microscopies) or by imaging the time-resolved photoluminescence (in the case of time-resolved photoluminescence microscopy).[6-8] While data collection specifics may vary among practitioners and for different materials systems, all methods directly image the excited state population's spatiotemporal evolution and provide quantitative measures of energy and/or charge transport. For the remainder of this manuscript, we will refer to this class of measurement techniques collectively as transport imaging.

Regardless of whether the excited state population is imaged via a pump-probe response or through photoluminescence, it is common practice to quantify excited state transport by a composite least squares fitting approach, illustrated in Fig. 1.[4, 7, 9] The first step of this composite fit extracts the mean squared width of the excited state distribution immediately following photoexcitation and at a series of fixed delays. Often, this profile is well-described by a Gaussian model.[10] The functional dependence of how the profile width changes with time is the key observable in transport imaging, as it is indicative of the physical processes that govern excited state transport. In the limit excited state transport is diffusive, the mean-squared displacement (MSD) of the distribution increases linearly with time and the diffusion coefficient can be determined from a linear fit to the time-dependent MSD derived from the

fitted Gaussian curves.[8, 11] For cases where transport deviates from this ideal scenario, the MSD of the excited state distribution can be fit to non-linear functions including power law diffusion, exponential transitions of linear diffusion regimes, trapping/detrapping models, or other numerical approaches.[8, 12-21]

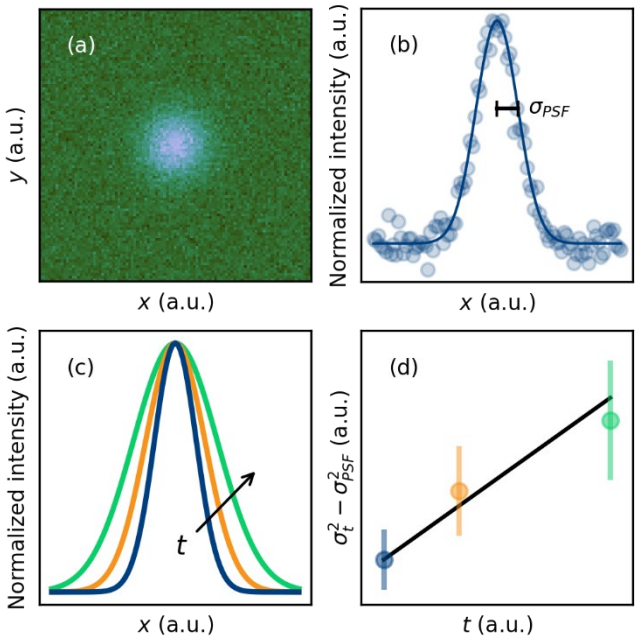

Figure 1: Illustration of the conventional two-step composite fitting procedure in optical measures of excited state transport. Panel (a) shows a modeled two-dimensional point-spread function typical of transport imaging, in which photoluminescence or a change in the optical constants reveals a distribution of photogenerated excited states. In this simulated example, the contrast-to-noise ratio (CNR) is 20. A cross section of the signal intensity is shown in panel (b). A fitted Gaussian function, blue solid line, yields the width parameter σ_{PSF}. In panel (c), additional profiles are collected at increasing delay times following photoexcitation, normalized to the peak amplitude, and fitted to Gaussian functions (gold, green solid lines). (d) The mean squared displacements ($\sigma_t^2 - \sigma_{PSF}^2$, blue, gold, and green circles with error bars) are fitted to a linear function where the slope is proportional to the diffusion coefficient.

It is generally acknowledged that the precision of a diffusion coefficient determined with transport imaging is primarily limited by uncertainties stemming from measurement noise.[4, 16, 22-25] Uncertainties in transport imaging manifest in two steps, reflecting the two-step approach to extracting a diffusion coefficient from experimental data. First, *spatial* uncertainty is conveyed as an error bar associated with the fit of the excited state distribution mean squared width for a particular time delay. In the second step, an overall confidence interval is provided for the diffusion coefficient, capturing the uncertainty associated with the *temporal* evolution of the excited state spatial distribution.[26-28] These two uncertainties,

presented separately, often stand as heuristic indicators of fit quality. While some researchers have provided statistical analyses of their results,[25, 28, 29] a systematic analysis of the extent to which noise impacts the precision and accuracy of diffusion estimates has not been reported. Consequently, it is difficult to evaluate whether a reported diffusion coefficient derived from a single data set is representative of the range of possible values caused by finite experimental noise. With the growing importance of optical methods in determining transport properties of materials,[1, 4, 6, 23, 30, 31] quantitative assessment of the ramifications of noise on such measurements is imperative.

To provide a quantitative evaluation of the impacts of noise on transport imaging, we model the diffusion and decay of excited state spatial distributions for a range of diffusion lengths, additive white noise amplitudes, and spatiotemporal resolutions. As is typically performed experimentally, the resultant time-dependent mean-squared displacements are fit to extract diffusion coefficient estimates. Comparisons of model outputs (*i.e.*, estimated diffusion coefficients) to the nominal inputs show surprising levels of imprecision, and in some cases systematic inaccuracies, to the extent that even qualitative comparisons of transport properties of materials are called into question with moderate levels of noise and common experimental parameters. For example, assuming a plausible set of experimental parameters – a diffusion length of 50 nm, an initial signal full-width-half-maximum ($FWHM_0$) of 1 μm, a spatial resolution of 20 pixels per $FWHM_0$, a temporal resolution of 10 frames per lifetime, and an initial peak amplitude-to-noise ratio (or contrast-to-noise ratio, CNR) of 50:1 – our results show fewer than one half of experimental measurements will recover a diffusion coefficient that is within 50% of the actual value. We also find significant systematic error in scenarios of small signal size and short diffusion length. For example, for a diffusion length of 10 nm and a CNR_0 of 10:1 (maintaining the other parameters), the

average fit-determined diffusion coefficient is overestimated by more than an order of magnitude.

To facilitate a more robust evaluation of transport imaging experimental conditions, we provide a means for practitioners to rapidly assess the likelihood that their experimentally determined diffusion coefficients are accurate, given a set of experimental parameters (resolution, noise, and diffusion length over one decay lifetime). We also make available an open-source software tool that can be customized for diverse experimental protocols to estimate noise and assess its impact on composite fitting precision. Lastly, we recommend that authors of transport imaging papers include not only standard experimental parameters (*e.g.*, spot size, excitation fluence), but also report contrast-to-noise ratios and a sufficient number of measurements for statistical analysis.

II. METHODS

A. Time-evolving excited state population

To generate time-dependent excited state spatial distributions, we adopt a simple 1-D model in which the excited state population, $n(x,t)$, is assumed to evolve with first order decay and isotropic normal diffusion, Eq. 1.

$$\frac{\partial n(x,t)}{\partial t} = -k_1 n - D\nabla^2 n \tag{1}$$

Here k_1 is the first order rate constant and D is the diffusion constant. Solving Eq. 1 for a point source at a position x_0, the population density is characterized by a Gaussian function that broadens and decays in amplitude over time, Eq. 2, with lifetime $\tau = {k_1}^{-1}$.

$$n(x,t) = \exp(-t/\tau)\frac{1}{\sqrt{4\pi Dt}}\exp\left[-\frac{(x-x_0)^2}{4Dt}\right] \tag{2}$$

The mean-squared displacement (MSD) of excited states in a Gaussian distribution is proportional to the diffusion coefficient D. The MSD is equivalent to the difference between

the Gaussian mean squared width at a specific time after photoexcitation (σ_t^2) and the initial mean squared width of the measurement point spread function (σ_{PSF}^2).[12]

$$MSD \equiv \sigma_t^2 - \sigma_{PSF}^2 = 2Dt \tag{3}$$

The experimentally convenient full width at half maximum ($FWHM$) of the signal profile is related to the mean squared width of a Gaussian via $\sigma^2 = FWHM^2/8\ln 2$.

B. Contrast to noise ratio

A common parameterization of noise in imaging sciences is contrast to noise ratio, $CNR = A/\sigma_N$, which relates the signal amplitude (A) given by the absolute difference between the signal peak and baseline, to the standard deviation of the noise (σ_N).[32-34] The amplitude parameter is time dependent in transport imaging, reflecting the diffusion and decay processes of the excited state population. For an initial Gaussian excited state distribution, the time dependent amplitude, $A(t)$ is given by Eq. 4, where A_0 is the initial signal amplitude, σ_{PSF}^2 is the initial point-spread function mean squared width, τ is the excited state lifetime, and D is the diffusion coefficient.

$$A(t) = A_0\sigma_{\mathrm{PSF}}\exp(-t/\tau)\,/(2Dt + \sigma_{\mathrm{PSF}}^2)^{1/2} \tag{4}$$

To parameterize the CNR for the modeled data, the initial profile amplitude is set at unity and additive white noise is applied to the initial and time-evolved simulated signal profiles. For each time frame, a pseudorandom number generator (with a fresh seed value) returns a normal distribution of values with arbitrary standard deviation and mean of zero, and the generated noise values are added to each spatial pixel in the simulated signal profile. Noise is generated using NumPy's PCG-64, an implementation of O'Neill's permutation congruential generator.[35, 36]

Although the modeled CNR can be determined based on input parameters, a robust method to estimate CNR is necessary for evaluation of experimental data. Our approach for estimating CNR uses a 1D profile (which could be, for example, a slice through the center of a 2D signal profile). After normalization, a unitary Fourier transform (FT) is performed on the data. In the FT of the data set, the signal is centered at zero frequency, and the noise generally lies at higher spatial frequencies. Noise is estimated by finding the root mean squared amplitude for frequencies that lie above the first local minimum after the signal peak. The ratio of the peak amplitude to the RMS noise provides an estimate of the experimental CNR.

C. Generalized model parameters

Unless otherwise specified, the modeling described in this manuscript uses the following parameters: the spatial width of the entire data domain (L_x) is set to 5 in relative units of initial profile width ($FWHM_0$); the number of pixels across the spatial domain (N_{pix}) is 100; the duration over which profiles are fit is one decay lifetime ($t/\tau = 1$); the number of observations over the duration (time frames, N_t) is 10; the initial signal amplitude (A_0) is unity; the initial profile width ($FWHM_0$) is unity; and the spatial offset of the initial profile (μ) is zero in relative units of $FWHM_0$. These parameters, chosen to be comparable to those found in relevant experimental literature, are summarized in Table I.

To simplify analysis of the described simulations, the influence of decay and diffusion on CNR is normalized by parameterizing the lifetime diffusion length L_D, which is dependent on both diffusion and decay. The diffusion length is formally the mean squared displacement (MSD) of the distribution at $t = \tau$, but the numerical constant is typically omitted, $L_D = \sqrt{D\tau}$.[4, 37] To facilitate comparison across many materials systems and experimental

apparatuses, this manuscript expresses the diffusion length in terms of the initial profile $FWHM_0$.

	Parameter	Symbol	Default value	Unit
spatial/temporal resolution	spatial width across domain	L_x	5	$FWHM_0$
	number of pixels	N_{pix}	100	pixels
	duration	t/τ	1	none
	number of time frames	N_t	10	frames
initial distribution	initial amplitude	A_0	1	arbitrary
	initial profile width	$FWHM_0$	1	arbitrary
	spatial offset	μ	0	$FWHM_0$

Table I: Generalized simulation parameters and their default values and units.

D. Composite fitting algorithm

Following the generation of a series of noisy profiles in a given simulation, each profile is fit using the Levenberg–Marquardt algorithm implemented in the Python SciPy wrapper of the MINPACK Fortran library[38, 39] to find the parameters of a Gaussian function that minimize the sum of the squares of the deviations. The fitted parameters are the Gaussian mean squared width σ^2, the amplitude A, and the spatial offset μ. Because background is typically subtracted from experimental data, the baseline offset was fixed at zero. For the fitting algorithm, a common set of reasonable bounds and initial guesses were applied to the entire set of simulations. These bounds and initial guesses are summarized in Table II.

Parameter	Lower bound	Upper bound	Initial guess
Variance ($\boldsymbol{\sigma^2}$)	$(L_x/N_{\mathrm{pix}})^2$	L_x^2	$L_x^2/16$
Amplitude (A)	0	$2A_{\max}$	$A_{\max}$
Mean (μ)	$-L_x/10$	$L_x/10$	0

Table II: Initial bounds and guesses for Gaussian fitting parameters where L_x is the length of the spatial domain, N_{pix} is the total number of spatial pixels, and A_{max} is the profile data maximum.

To determine the diffusion coefficient, the MSD array – *i.e.*, the series of σ_t^2 parameters estimated by the Gaussian fits – is fit to Eq. 3. Both ordinary (i.e., unweighted) least squares and weighted least squares fits are compared. For weighted fitting (used in all cases except where otherwise indicated), normalized weights are calculated by the reciprocal of the relative variance of the mean squared width parameters from the Gaussian fits. To characterize both precision and accuracy of diffusion estimates, the results are described in terms of the portion of fits that are within a given proximity to the nominal input value.

III. RESULTS & DISCUSSION

A. Noise and Spatial Uncertainty

Transport imaging of a diffusive process generally proceeds via a two-step composite fitting procedure. The first step fits individual profiles to a model, often Gaussian, and the second step fits a linear model to the time-dependent mean squared profile widths. It is therefore essential to assess how error propagates through these two interconnected steps. In Figure 2, we examine step one of this composite fit. With CNR of 50, Fig. 2(a), profiles are well-fitted, with all fits yielding profile mean squared width estimates (σ_{est}^2) within 10% of the nominal parameter (σ_{nom}^2) input to the model, Fig. 2(b). The portion of good fits rapidly decreases below CNR of 20; but even for a CNR of 1 (*i.e.*, where the contrast is the same magnitude as the standard deviation of the noise), about 60% of fitted mean squared width estimates are still within 10% of the nominal value. These low CNR fits are artificially precise, reflecting the influence of the fitting constraints (see Table II). Figure 2(c)

summarizes these results, showing the fraction of Gaussian fits with an estimated mean squared width that lies within 10% of the nominal value when CNR is between 1 and 20. It is worth noting that fits to the full image (Fig. 1a) with a two dimensional Gaussian improves fit performance over a 1D Gaussian because the increased number of data points constrain the fit. However, for cases in which transport is known to be isotropic or is only of interest along one direction, larger performance gains are obtained by collecting a single 1D profile multiple times (and averaging to improve CNR) or by spatial oversampling (see discussion below) than by collecting a full 2D image.

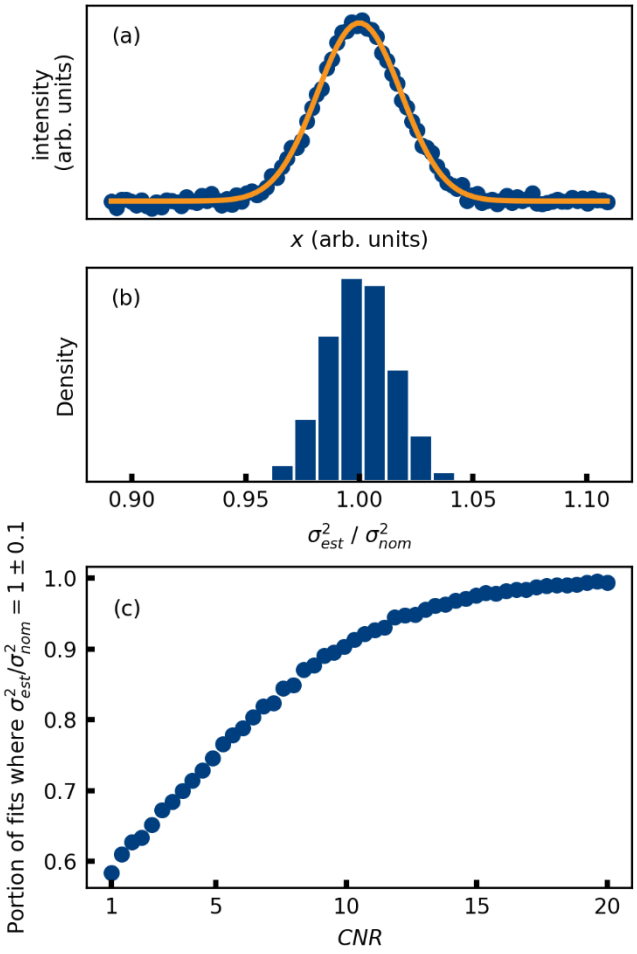

Figure 2: Gaussian fitting performance on noisy profiles with resolution of 20 pixels per $FWHM$ and a domain 5 times the length of $FWHM$. (a) Example Gaussian fit (gold solid) of a simulated profile with $CNR = 50$ (blue circles). (b) Histogram showing the relative proximity of 10,000 mean squared width estimates to the nominal value. (c) Portion of fitted mean squared width estimates, σ^2_{est}, within 10% of the nominal value, σ^2_{nom}, as a function of $1 \leq CNR \leq 20$. Each of the 100 scatter points in panel (c) represents 10,000 fits.

The bounds imposed on the width parameter (σ^2_{est}) of the Gaussian model described above led us to evaluate how fitting biases of low CNR profiles could propagate into the second step of the composite fit. While such low CNR fits are not common, they can become increasingly relevant at late delay times, when a significant portion of the photogenerated population has decayed. Figure 3 shows results from 100,000 individual fits of simulated profiles for CNR values of 20 (a), 5 (b), and 2 (c). Best-fit width (σ^2_{est}) parameters along with their standard errors (SE) calculated from the covariance matrix are shown as histograms. Also shown is the standard deviation (SD) directly calculated from the distribution of fit-determined σ^2_{est} values. For profiles with $CNR \gtrsim 5$ (Figs. 3a, b), distributions of σ^2_{est} values are unbiased and symmetric around the nominal modeled width, σ^2_{nom}. SE values reported by individual least squares fits are closely comparable to the SD of the distribution. While there are cases where the SE estimate from a single fit deviates from the SD of the population, generally these results show that, on average, the least squares fit provides an unbiased estimate of the parameter mean value and uncertainty. However, at very low CNR ($CNR \lesssim 5$, Fig. 3c), the Gaussian least-squares fit leads to two sources of bias. First, the SE determined from the covariance matrix underestimates the SD of the population by $\sim$20%. This discrepancy is a result of the Gaussian model which restricts $\sigma^2_{\mathrm{est}} > 0$. Because the model cannot be linearized in this limit, the SE calculated from the covariance matrix is incorrect.[40] Second, the average of the width estimates ($\langle\sigma^2_{\mathrm{est}}\rangle$) is more than 5% higher than σ^2_{nom}, while the median of σ^2_{est} is about 3% below the nominal value. This difference between the mean and the median indicates a skewing of the σ^2_{est} distribution toward larger widths at low CNR. As discussed and shown below (Fig. 7), The skewness of the distribution of σ^2_{est} distribution leads to systematic errors in diffusion constant estimation at low CNR.

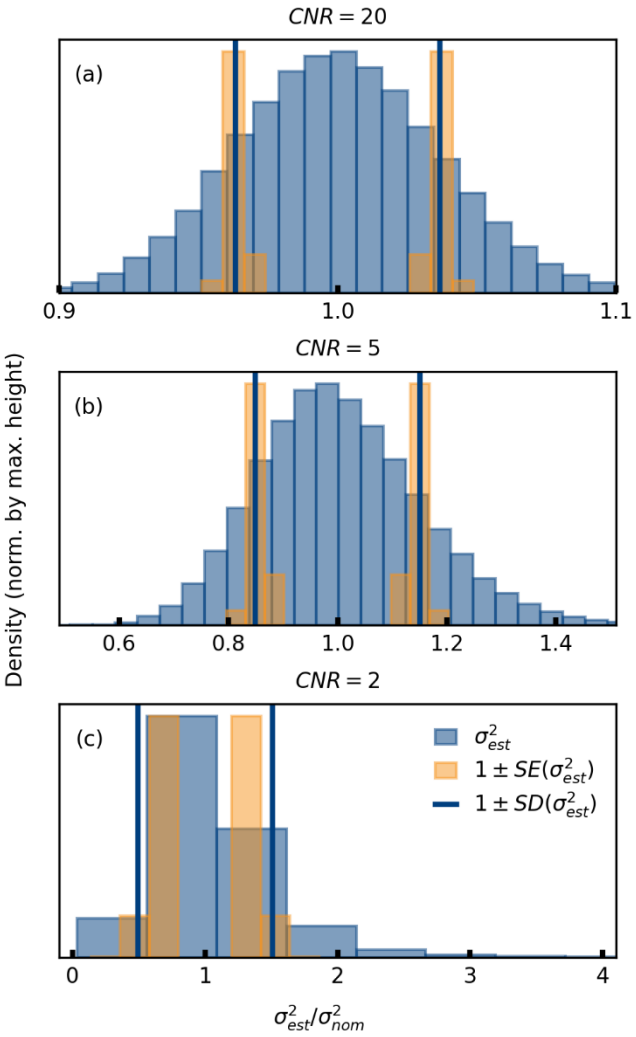

Figure 3: Comparison between standard deviation (SD, solid blue vertical bars) of fitted mean squared width estimates (σ^2_{est}, blue histogram bars) and the standard error (SE, gold histogram bars) as given by the fitting algorithm. The profile widths, SD, and SE are all normalized against the nominal profile mean squared width parameter (σ^2_{nom}). The distributions shown on each panel were derived from 100,000 simulated Gaussian profiles with additive white noise. Histograms are normalized to the highest bars for visual comparison. (a) Results for $CNR = 20$. No skewness is apparent in the distribution of σ^2_{est}, with mean and median both being 1.000. The SD and mean standard error of σ^2_{est} ($\overline{SE}$) are both equal to 0.037. (b) Results for $CNR = 5$. Slight skewness is apparent in the distribution of σ^2_{est}, with mean of 1.006 and median of 0.995. The SD and $\overline{SE}$ are near agreement with $SD = 0.150$ and $\overline{SE} = 0.146$. (c) Results for $CNR = 2$. The distribution of σ^2_{est} is skewed right due to many outliers with large values, with mean of 1.054 and median of 0.968. The SD of σ^2_{est} is 0.507, but $\overline{SE} = 0.364$, showing an underestimation of the error calculated by the fitting algorithm.

B. Noise and Estimation of *D*

In the limit transport is well described by normal diffusion, the mean squared width (σ_t^2) of the excited state spatial profile increases linearly with time after photoexcitation. A set of fit-determined MSDs can therefore be linearly fit to find the diffusion coefficient. Figure 4(a) illustrates this procedure for a representative series of data modeled with initial contrast to

noise ratio, $CNR_0 = 50$, and a diffusion length, $L_D = 0.1\ FWHM_0$. The blue solid line shows the best linear fit to the MSD data obtained from least squares fits of time-dependent profiles. The gold line shows the slope of theoretical σ_t^2 values, which is proportional to the nominal diffusion coefficient input to the model. The difference in slope between the two lines is a consequence of the cumulative uncertainty in mean squared widths associated with random noise and decreasing signal amplitude due to diffusion and single exponential decay (Eqs. 2, 4).

For a given diffusion length and CNR_0, the precision of the composite fitting procedure can be characterized by the spread of the diffusion constant estimates. Fig. 4(b) shows the results of linear fits to 1000 data sets (like those shown in Fig. 4a), each simulated with $CNR_0 = 100$, and $L_D = 0.1\ FWHM_0$. A histogram of the fit-determined diffusion coefficients from these 1000 simulations, normalized to the model input parameter, D_{nom}, is shown in Fig. 4(c). For this high-contrast example with moderate diffusion length, 96% of the estimates are within 50% of the nominal diffusion coefficient.

A challenge of the composite fitting approach is that both diffusion and excited state relaxation cause a decrease in the CNR with time, which in turn leads to profile fits whose uncertainty increases with time. This noise variability in a dataset, called heteroscedasticity, has been previously identified as a confounding factor in the analysis of imaging spectroscopy, transient kinetics, and lifetime imaging.[41-43] When the uncertainty of measurements changes monotonically over time, the ratio of final to initial CNR is a simple way to characterize heteroscedasticity. For a one-dimensional Gaussian profile with arbitrary initial RMS width σ_{PSF} and an excited state diffusion length L_D under first-order decay, the time-dependent decrease in contrast is a function of diffusion length, L_D, and time as a fraction of lifetime, t/τ, Eq. 5.

$$CNR_{t/\tau}/CNR_0 = \sigma_{\mathrm{PSF}} \exp(-t/\tau)/(2L_D^2(t/\tau) + \sigma_{\mathrm{PSF}}^2)^{1/2} \quad (5)$$

Examination of Eq. 5 shows that amplitude is diminished (assuming noise is constant) by a factor that scales exponentially with time and as $1/L_D$ (for large L_D).

One strategy for mitigating the impacts of heteroscedasticity is to use weighted fitting in the second step of the composite fitting procedure. Figure 4(d) compares the precision of weighted and unweighted composite fitting as a function of L_D for an initial CNR_0 = 50. While the performance of both approaches quickly diminishes for $L_D < 0.1\ FWHM_0$, the weighted approach does provide better precision across the range. For moderate L_D from about 0.1 to 1.0 $FWHM_0$, both approaches yield estimates that all are within 50% of the nominal diffusion coefficient. In cases of high diffusion length, $L_D > 1.0\ FWHM_0$, the unweighted fit performs worse again, due to the rapid loss of contrast from diffusion. As will be discussed later, weighting the fit does not always fully correct more extreme cases where contrast diminishes quickly. Figure 4(e) compares weighted and unweighted fitting methods as a function of CNR_0 for an $L_D = 0.1\ FWHM_0$. Here again, the weighted approach provides a small, but consistent improvement across the range of CNR_0 values. In fact, in our modeling of 2 million diffusion trajectories with $3.33 \leq CNR_0 \leq 100$ and $0.01 \leq L_D \leq 20\ FWHM_0$, a collection of weighted fits was never found to be *less* precise than the corresponding collection of unweighted fits. Given the ease with which weights are calculated (see section IIB) there is, as far as we can determine, no reason *not* to implement weighted fits in the linear fit of time-evolved mean squared widths of excited state population distributions in transport imaging data.

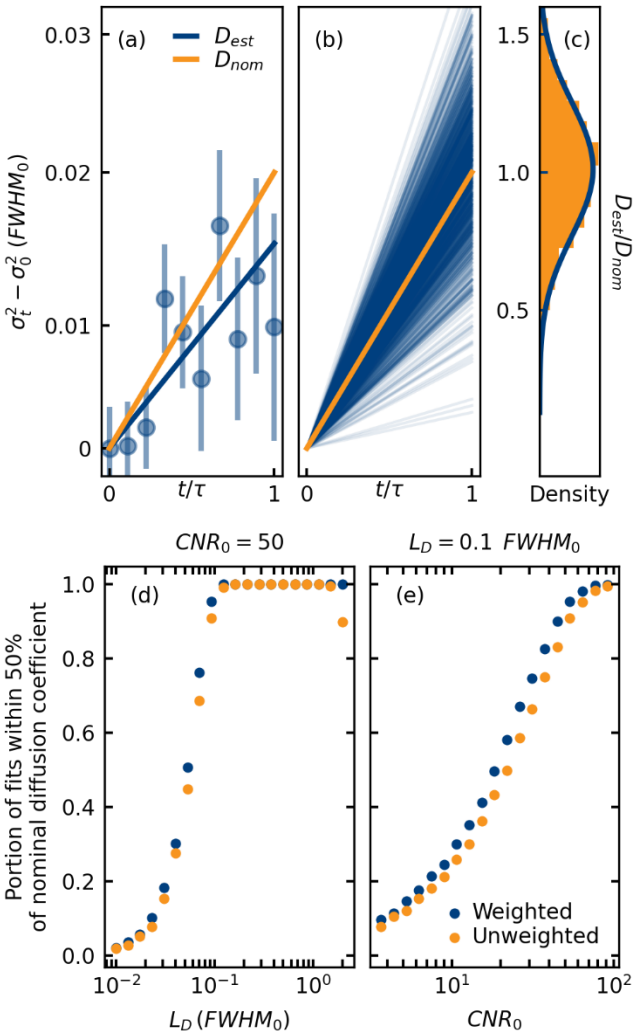

Figure 4: Composite fitting and comparison between weighted and unweighted linear fit performance with a domain width of 5 times $FWHM_0$, pixel resolution of 20 per $FWHM_0$, and temporal resolution of 10 per decay lifetime. Displacement is normalized to the diffusion length and time normalized to the lifetime. Panels a), b) and c) present data for $L_D = 0.1\ FWHM_0$ and $CNR_0 = 50$. (a) Simulated data showing 10 uniformly-timed mean-squared displacements of the excited state spatial profile with added white noise, fitted as MSD relative to the initial Gaussian mean squared width ($\sigma_t^2 - \sigma_0^2$) (circles). Error bars show the relative standard error of the fitted mean squared width. The blue solid line shows a linear fit to the data to extract D_{est}. The gold line shows the slope corresponding to the nominal diffusion coefficient (D_{nom}). (b) Linear fits from 1000 simulations. (c) Histogram of fitted diffusion coefficients relative to the nominal value (D_{est}/D_{nom}), with a normal curve fitted to the histogram (blue). Panels d) and e) present the portion of fitted diffusion coefficients that fall within 50% of the nominal value, ($D_{est}/D_{nom} = 1 \pm 0.5$), contrasting the performance of weighted (blue) and unweighted (gold) linear fits of the Gaussian mean squared width over one lifetime. (d) $CNR_0 = 50$ and $0.01\ FWHM_0 \leq L_D \leq 2.0\ FWHM_0$, and (e) $3.33 \leq CNR_0 \leq 100.0$ and $L_D = 0.1\ FWHM_0$. Each data point in panels d) and e) represents the result from 5000 fits.

While many factors affect the robustness of transport imaging, the most important parameters are the excited state diffusion length, L_D and the contrast to noise ratio, CNR. To provide more comprehensive insight into how these two parameters affect the precision and accuracy afforded by the composite fitting procedure, simulations and fitting were performed

for 20 diffusion lengths between 0.01 and 2.0 $FWHM_0$, over a range of 100,000 randomly selected CNR_0 values, collected in 20 bins between 3.33 and 100. The range of these parameters encompasses the vast majority of published experimental work in this area. For each diffusion length and CNR_0 bin, 5,000 simulations were performed. The results are summarized in Fig. 5, which shows the fraction of diffusion constant estimates within 50% of the nominal value.

Not surprisingly, Fig. 5 shows that measurements with longer diffusion lengths under conditions of higher CNR_0 are generally more precise and accurate. For example, 90% of fits recover a diffusion estimate, $D_{\mathrm{est}}/D_{\mathrm{nom}} = 1 \pm 0.5$ when the diffusion length is more than $\sim 0.1\ FWHM_0$ and $CNR_0 \gtrsim 40$. For longer diffusion lengths up to $\sim 1.0\ FWHM_0$, noise is better tolerated, with the same precision holding at CNR_0 as low as ~ 6. For diffusion lengths greater than $\sim 1.0\ FWHM_0$, as we also saw in Fig. 3(d), the trend of greater noise tolerance reverses, reflecting the rapid loss in CNR due to diffusion (Eqs. 2, 5) at times that approach one lifetime. Note however, that the deleterious effects of rapid diffusion on CNR can be easily mitigated by collecting data for delay times $\ll \tau$.

Whether stemming from a short excited-state lifetime or from a small diffusion coefficient, the precision of transport imaging drops sharply for diffusion lengths shorter than $\sim 0.1\ FWHM_0$, as evidenced by the density of contours in Fig. 5. This rapid loss in precision primarily derives from the fact that the mean-squared displacement (due to transport) is similar in magnitude to the standard error of the fitted profile width. Under these conditions, the distribution of linear fits can be very large. For example, if it is desired to resolve $L_D = 0.05\ FWHM_0$ (*e.g.*, a 50 nm diffusion length for a 1 μm spot size), one needs an initial $CNR_0 \gtrsim 70$ just to ensure that half of the performed transport imaging measurements will recover a D_{est} within 50% of the actual diffusion coefficient of the material. If a better degree

of accuracy were needed for a particular research goal, the CNR requirements are clearly more stringent.

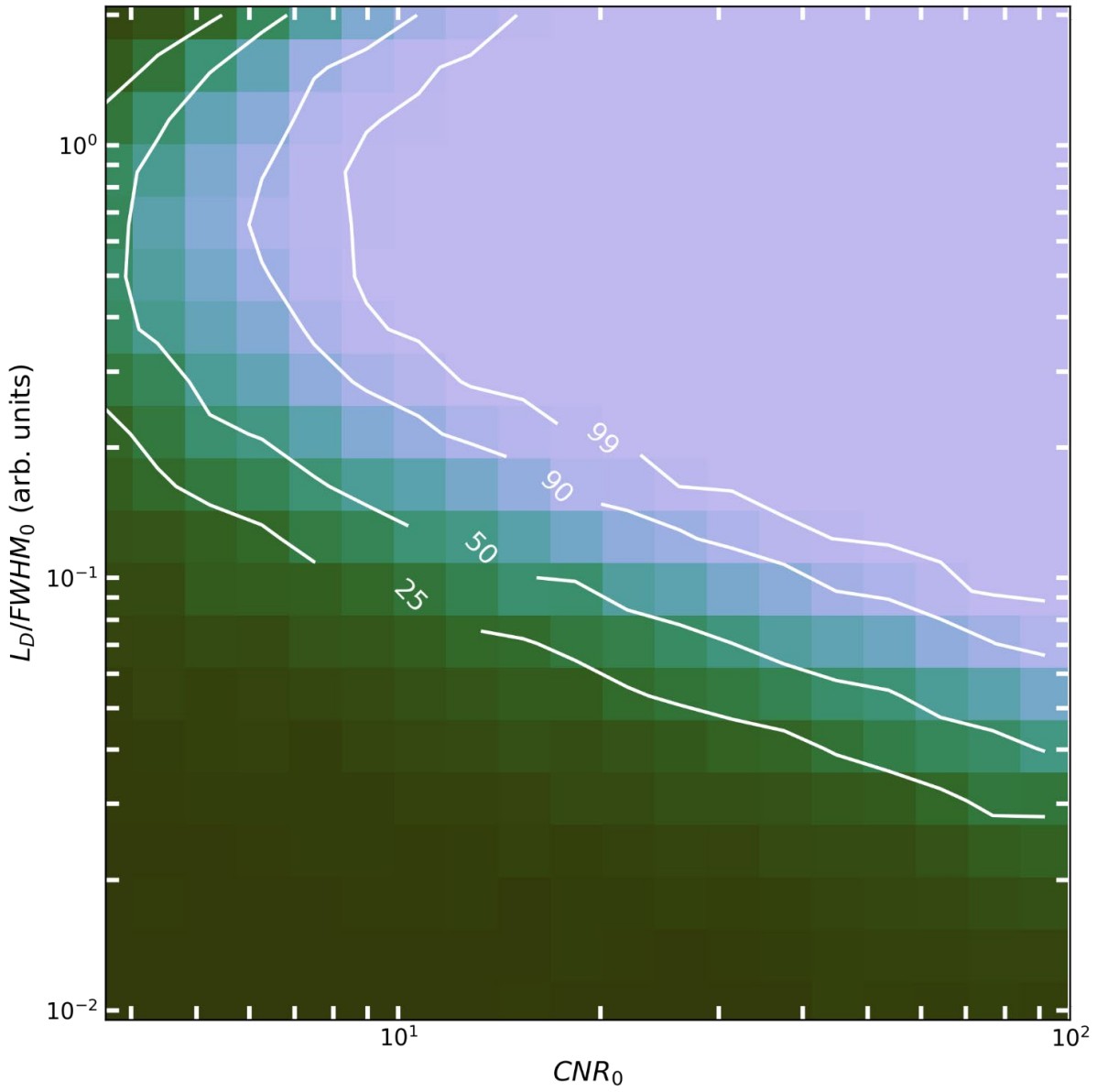

Figure 5: Proximity of diffusion coefficient estimates (D_{est}) to the nominal input values (D_{nom}) as a function of initial contrast-to-noise ratio (CNR_0) and lifetime diffusion length relative to initial profile full width half-maximum ($FWHM_0$). Contours indicate the percent of fitted diffusion coefficient estimates where $D_{est}/D_{nom} = 1 \pm 0.5$ All fitted linear functions to derive diffusion constant estimates were weighted by the reciprocal of the relative variance of the mean squared width parameters from the Gaussian fits.

For many relevant materials systems, particularly those with strong coupling between electronic and nuclear degrees of freedom, the diffusion length may be $\lesssim$ 10 nm, which corresponds approximately to the lower limit of Fig. 5 for typical diffraction limited

experimental conditions ($FWHM_0 \sim 1$ μm). The conditions assumed in the generation of Fig. 5, where $N_{\mathrm{pix}} = 100$ and $N_t = 10$, are insufficient to accurately measure such small diffusion lengths. For these scenarios, it is important to consider what steps can be taken to improve measurement fidelity. Figure 6 summarizes how increasing CNR_0 and spatial (N_{pix}) and temporal (N_t) oversampling can be leveraged to improve measures of D_{est} for a diffusion length of $L_D = 0.01\ FHWM_0$. Not surprisingly, temporal and/or spatial oversampling improves the accuracy of individual fits and the precision of fit-determined D_{est} values, reflected by a decrease in the width of the distribution of estimates. However, like increases to the CNR obtained by signal averaging, the improved performance comes at the expense of increased measurement time. Indeed, the precision improvement of fit-determined D_{est} values due to spatial and temporal oversampling generally scales as $\sqrt{N}$, where N is the number of spatial pixels or time frames collected (see for example, the $\sim\sqrt{10}$ improvement in fit performance for a $CNR_0 = 100$ from panels a to c).

In terms of measurement duration, the $\sqrt{N}$ scaling matches what can be achieved in shot-noise-limited signal averaging, suggesting that spatial or temporal oversampling doesn't provide any advantage over improvements in CNR. It is worth noting, however, that widefield detection (rather than single point scanning detection) enables spatial oversampling without increases to measurement time, provided a sufficient photon flux can be realized.[24, 28, 29] Moreover, depending on experimental parameters (primary noise source, sample sensitivity, photon flux, etc.), improvements in transport imaging via oversampling may be more practical than simply improving CNR via signal averaging. Experimental modifications can also help overcome noise limitations.[44] Nevertheless, for the extreme case in which $L_D = 0.01\ FHWM_0$, even with a spatial resolution of 800 pixels per $FWHM_0$ and 400 time frames sampled within one recombination lifetime, the CNR_0 must still be at least 100 to ensure 90%

of fits recover diffusion constants within 50% of the nominal value. These experimental conditions are exceptionally challenging to achieve, suggesting that the most practical strategy is to decrease spot size (*i.e.,* move vertically in Fig. 5), which improves fit quality as approximately $FWHM_0^{-2}$.

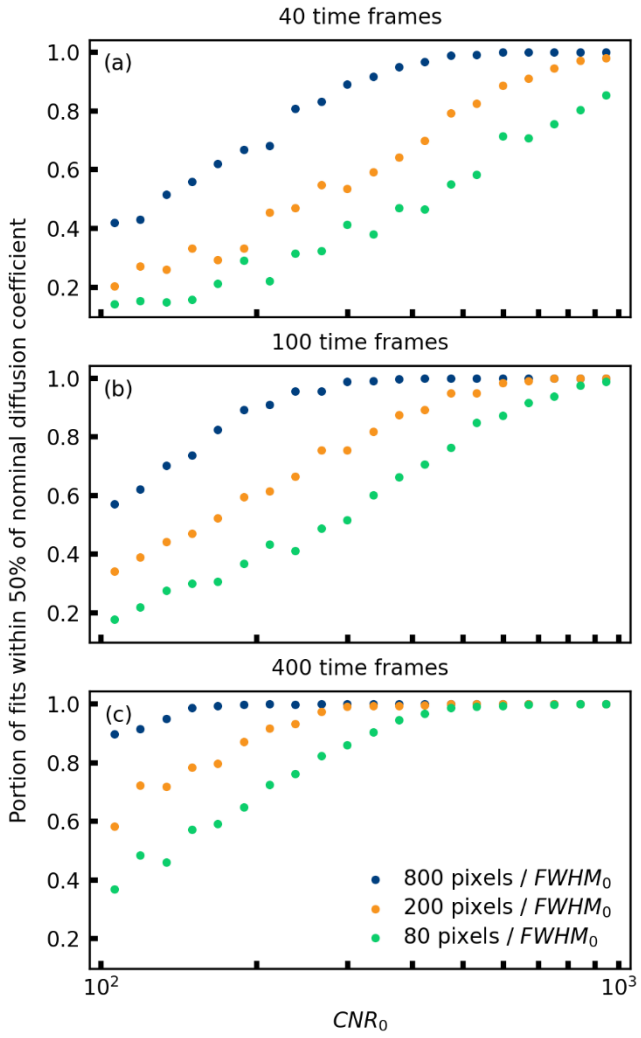

Figure 6: Variations in spatial and temporal resolution for a simulation with diffusion length of $0.01\ FWHM_0$*, duration of one lifetime, and spatial domain width of* $5\ FWHM_0$ *over a range of* CNR_0 *values between 100 and 1000. Increasing the number of spatial pixels or temporal frames improves the precision of diffusion coefficient estimates. (a) 40 time frames, (b) 100 time frames, (c) 400 time frames.*

Up to this point, we have discussed how noise introduces random error in fit-determined D_{est} values, *i.e.*, how wide the distribution of D_{est} values is relative to D_{nom} for a set of measurement parameters. However, we have not yet considered whether noise can lead to systematic error in the *average* of the fit-determined D_{est} values ($\langle D_{\mathrm{est}} \rangle$). Figures 7(a) and

7(b) explore the effect of random noise on systematic error propagated through the composite fitting approach. In Fig. 7(a), $\langle D_{\mathrm{est}} \rangle$ normalized to D_{nom}, is plotted as a function of L_D assuming an atypical $CNR_0 = 10$ for illustration. For these simulations, $\langle D_{\mathrm{est}} \rangle$ is calculated by averaging 10,000 individual fit-determined D_{est} values for L_D ranging between $0.01\ FWHM_0$ and $2.0\ FWHM_0$. There is no systematic error for large diffusion lengths, however for $L_D \leq 0.1\ FWHM_0$, the mean estimated diffusion coefficient, $\langle D_{\mathrm{est}} \rangle$, is biased toward faster diffusion rates. In the extreme case of low contrast *and* small diffusion length, $L_D = 0.01\ FWHM_0$, the 5,000 runs of the composite least squares fitting routine yields a $\langle D_{\mathrm{est}} \rangle$ that is an order of magnitude larger than D_{nom}. Figure 7(b) explores systematic error as a function of CNR_0 for an $L_D = 0.1\ FWHM_0$. Here systematic error begins to bias the $\langle D_{\mathrm{est}} \rangle$ at $CNR_0 \lesssim 10$.

The systematic error introduced by the composite fitting approach arises primarily because low CNR results in instances wherein the profile width is significantly overestimated, as illustrated in Fig. 3(c). A compounding factor is that in these cases, the least squares fit underestimates the uncertainty of the determined width parameter if the SE is determined directly from the covariance matrix diagonals. Both effects lead to estimates of the diffusion coefficient that skew $\langle D_{\mathrm{est}} \rangle$ to values that are systematically larger than D_{nom}. These results indicate that it is inadvisable to simply find the mean of multiple composite regression-derived fits of diffusion coefficients, at least when one is trying to measure small diffusion constants with relatively low CNR_0. Instead, it is more robust to average the data across multiple measurements initially, thus reducing noise, before proceeding with the composite fitting procedure.

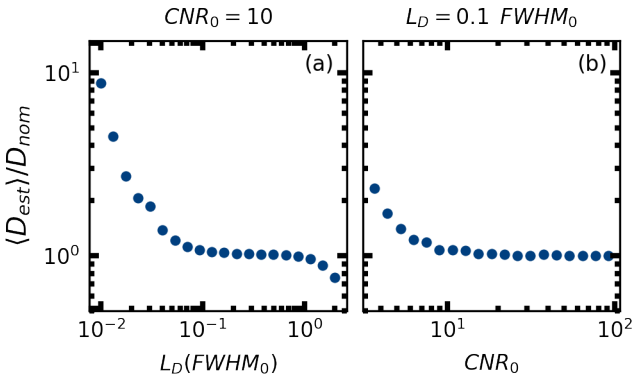

Figure 2: Composite fitting bias in the limit of low contrast and small diffusion length. Bias is defined as the ratio of the mean diffusion estimate to the nominal diffusion coefficient. Panel (a) shows bias as a function of diffusion length for $CNR_0 = 10$, and panel (b) presents bias as a function of CNR_0 for $L_D = 0.1\ FWHM_0$. Each point on these plots represents results from 5,000 simulations and composite fitting procedures.

IV. CONCLUSION

In this work we have quantified the impact of noise on optical methods of estimating diffusion coefficients through composite least squares fitting. We have shown that noise can have a profound influence on the precision of diffusion estimates, depending on many experimental parameters which can, in some combinations, synergistically magnify measurement uncertainty. The parameters that contribute to the influence of noise include the contrast-to-noise ratio itself, the magnitude of diffusion over the experiment duration, the decay of contrast due to excited-state recombination and diffusion (*i.e.*, heteroscedasticity), the initial mean squared width of the excited state population distribution, and the temporal and spatial resolution of measurements. Noise can add great uncertainty to estimates of diffusion coefficients even in the most idealized scenario of excited state profiles being well-fitted by Gaussian functions, diffusion being isotropic, mean-squared displacement increasing linearly, and first-order recombination, to such an extent that even qualitative comparisons of transport mechanisms may be suspect under some sets of experimental parameters. Analytical approaches employing other profile fitting functions, non-linear diffusion functions, or phenomenological models may be even more sensitive to noise.

Not surprisingly, poor precision in diffusion estimates primarily arises under conditions when the standard error for each fitted profile is of similar magnitude to, or larger than the displacement over the experiment time. This intrinsic noise can lead to diffusion estimates that are imprecise, substantiating the general understanding that noise is the principal limiting factor in estimates of excited state diffusion. It is important to recognize, however, that some variability in determined diffusion coefficients is intrinsic to the measurement under all experimental conditions, and it should therefore be standard practice to report CNR_0 and provide a sufficient number of determined diffusion coefficients to evaluate their statistical significance. However, under experimental parameters where estimates have systematic error, no number of estimates will be sufficient to evaluate their significance.

Several strategies can be undertaken to mitigate the effects of noise. Increasing the initial CNR is perhaps the most obvious approach, which can be accomplished by improvements to instrumentation, or by averaging multiple measurements at a given time frame. In the case of slow diffusion, the impact of noise can be abated by collecting data at later times so that the MSD of the excited state population is comparable to $FWHM_0$. Care must be taken, however, that the contrast does not diminish too greatly over the course of the experimental time. Also, spatial and/or temporal oversampling can provide better estimates at the expense of increased measurement time. The effects of heteroscedasticity can be diminished by using weighted least squares linear regression to estimate the diffusion coefficient in the second step of the composite fitting approach. Care should be taken, however, for profiles with $CNR_t \lesssim 5$ because fits of noisy profiles have under-estimated uncertainty from standard least square algorithms and are therefore over-weighted in step 2 of the composite fit. Moreover, when measuring small diffusion lengths with low initial CNR, it is crucial to avoid averaging fitted diffusion coefficients that may be systematically over-estimated, and instead first reduce noise through averaging of individual profile images.

Performing simulations in advance can clarify what changes to experimental parameters, if any, may be fruitful. Therefore, we have created an open-source software tool for practitioners to simulate diffusion measurement experiments and evaluate the precision of diffusion coefficient estimates resulting from a set of arbitrary experimental parameters. The tool is available for download with full documentation.[45] It provides easy access to modify all the parameters discussed herein, and can be further developed to include additional terms for higher order recombination, phenomenological perturbations of the idealized case, or to include other fitting models like bivariate Gaussian profiles, Voigt profiles, power law diffusion, *etc.* Moreover, the function to estimate the contrast to noise ratio of a 1-dimensional profile, described in Section IIB, is available to use immediately on the web without installing Python.

Because of the large parameter space and varying goals of researchers, it is impossible to summarize the precision that can be expected in every possible scenario in this work. The quantification of the impact of noise represented herein presumes that diffusion estimates within 50% of the nominal value are sufficiently accurate. It may be that better accuracy is necessary, or that lower accuracy can be tolerated, for a particular research project. Regardless, it is evident that the confidence with which optical measures of excited state transport are reported must be informed by more robust analysis than a set of error bars on a series of fitted Gaussian variances, as this method fails to capture the intrinsic uncertainty present with this technique.

ACKNOWLEDGEMENTS

This material is based upon work supported by the National Science Foundation under award No. 2154448.

AUTHOR DECLARATIONS

Conflict of Interest

The authors have no conflicts to disclose.

Author Contributions

Joseph J. Thiebes: Conceptualization (equal); data curation (lead); formal analysis (equal); investigation (lead); methodology (lead); resources (supporting); software (lead); validation (lead); visualization (lead); writing – original draft (lead); writing – review and editing (equal). **Erik M. Grumstrup**: Conceptualization (equal); formal analysis (equal); funding acquisition (lead); investigation (supporting); methodology (supporting); project administration (lead); resources (lead); supervision (lead); writing – original draft (supporting); writing – review and editing (equal).

DATA AVAILABILITY

The data that support the findings of this study are available from the corresponding author upon reasonable request.

REFERENCES

1. P.-T. Dong, and J.-X. Cheng, *Spectroscopy* **32**, 24 (2017).

2. H. Wen, M. J. Cherukara, and M. V. Holt, *Annual Review of Materials Research* **49**, 389 (2019). https://doi.org/10.1146/annurev-matsci-070616-124014

3. T. Zhu, J. M. Snaider, L. Yuan, and L. Huang, *Annual Review of Physical Chemistry* **70**, 219 (2019). https://doi.org/10.1146/annurev-physchem-042018-052605

4. N. S. Ginsberg, and W. A. Tisdale, *Annual Review of Physical Chemistry* **71**, 1 (2020). https://doi.org/10.1146/annurev-physchem-052516-050703

5. Y. Zhu, and J.-X. Cheng, *The Journal of Chemical Physics* **152**, (2020). https://doi.org/10.1063/1.5129123

6. M. C. Fischer, J. W. Wilson, F. E. Robles, and W. S. Warren, *Review of Scientific Instruments* **87**, 031101 (2016). https://doi.org/10.1063/1.4943211

7. S. Deng, D. D. Blach, L. Jin, and L. Huang, *Adv Energy Mater* **10**, 1903781 (2020). https://doi.org/10.1002/aenm.201903781

8. D. W. deQuilettes, R. Brenes, M. Laitz, B. T. Motes, M. M. Glazov, and V. Bulović, *ACS Photonics* **9**, 110 (2021). https://doi.org/10.1021/acsphotonics.1c01186

9. C. Stavrakas, G. Delport, A. A. Zhumekenov, M. Anaya, R. Chahbazian, O. M. Bakr, E. S. Barnard, and S. D. Stranks, *Acs Energy Lett* **5**, 117 (2020). https://doi.org/10.1021/acsenergylett.9b02244

10. B. Zhang, J. Zerubia, and J.-C. Olivo-Marin, *Applied Optics* **46**, 1819 (2007). https://doi.org/10.1364/AO.46.001819

11. G. M. Akselrod, P. B. Deotare, N. J. Thompson, J. Lee, W. A. Tisdale, M. A. Baldo, V. M. Menon, and V. Bulović, *Nature Communications* **5**, (2014). https://doi.org/10.1038/ncomms4646

12. G. M. Akselrod, F. Prins, L. V. Poulikakos, E. M. Lee, M. C. Weidman, A. J. Mork, A. P. Willard, V. Bulovic, and W. A. Tisdale, *Nano Lett* **14**, 3556 (2014). https://doi.org/10.1021/nl501190s

13. W. Li, M. S. R. Huang, S. K. Yadavalli, J. D. Lizarazo Ferro, Y. Zhou, A. Zaslavsky, N. P. Padture, and R. Zia, *ACS Photonics* **6**, 2375 (2019). https://doi.org/10.1021/acsphotonics.9b00778

14. A. Sridharan, N. K. Noel, H. Hwang, S. Hafezian, B. P. Rand, and S. Kéna-Cohen, *Physical Review Materials* **3**, (2019). https://doi.org/10.1103/physrevmaterials.3.125403

15. E. M. Van Goethem, C. W. Pinion, E. E. M. Cating, J. F. Cahoon, and J. M. Papanikolas, *ACS Photonics* **6**, 2213 (2019). https://doi.org/10.1021/acsphotonics.8b01736

16. C. L. Hickey, and E. M. Grumstrup, *The Journal of Physical Chemistry C*, (2020). https://doi.org/10.1021/acs.jpcc.0c02302

17. E. Penzo, A. Loiudice, E. S. Barnard, N. J. Borys, M. J. Jurow, M. Lorenzon, I. Rajzbaum, E. K. Wong, Y. Liu, A. M. Schwartzberg, S. Cabrini, S. Whitelam, R. Buonsanti, and A. Weber-Bargioni, *ACS Nano* **14**, 6999 (2020). https://doi.org/10.1021/acsnano.0c01536

18. M. Seitz, A. J. Magdaleno, N. Alcázar-Cano, M. Meléndez, T. J. Lubbers, S. W. Walraven, S. Pakdel, E. Prada, R. Delgado-Buscalioni, and F. Prins, *Nature Communications* **11**, 1 (2020). https://doi.org/doi:10.1038/s41467-020-15882-w

19. M. Seitz, M. Meléndez, N. Alcázar-Cano, D. N. Congreve, R. Delgado-Buscalioni, and F. Prins, *Advanced Optical Materials*, 2001875 (2021). https://doi.org/10.1002/adom.202001875

20. J. Li, Z. Chen, S. Saha, J. K. Utterback, M. L. Aubrey, R. Yuan, H. L. Weaver, N. S. Ginsberg, K. W. Chapman, M. R. Filip, and H. I. Karunadasa, *Journal of the American Chemical Society* **144**, 22403 (2022). https://doi.org/10.1021/jacs.2c09382

21. N. Nagaya Wong, S. K. Ha, K. Williams, W. Shcherbakov-Wu, J. W. Swan, and W. A. Tisdale, *The Journal of Chemical Physics* **157**, 104201 (2022). https://doi.org/10.1063/5.0100075

22. S. Chong, W. Min, and X. S. Xie, *The Journal of Physical Chemistry Letters* **1**, 3316 (2010). https://doi.org/10.1021/jz1014289

23. Z. Guo, J. S. Manser, Y. Wan, P. V. Kamat, and L. Huang, *Nature Communications* **6**, 7471 (2015). https://doi.org/10.1038/ncomms8471

24. M. Delor, H. L. Weaver, Q. Yu, and N. S. Ginsberg, *Nature Materials* **19**, 56 (2020). https://doi.org/10.1038/s41563-019-0498-x

25. M. I. Saidaminov, K. Williams, M. Wei, A. Johnston, R. Quintero-Bermudez, M. Vafaie, J. M. Pina, A. H. Proppe, Y. Hou, G. Walters, S. O. Kelley, W. A. Tisdale, and E. H. Sargent, *Nature Materials* **19**, 412 (2020). https://doi.org/10.1038/s41563-019-0602-2

26. Z. Guo, Y. Wan, M. Yang, J. Snaider, K. Zhu, and L. Huang, *Science* **356**, 59 (2017). https://doi.org/10.1126/science.aam7744

27. Y.-K. Zhou, X.-Z. Li, Q.-N. Zhou, R.-H. Xing, Y. Zhang, B. Bai, H.-H. Fang, and H.-B. Sun, (2022). https://doi.org/0002

28. Z. Zhang, J. Sung, D. T. W. Toolan, S. Han, R. Pandya, M. P. Weir, J. Xiao, S. Dowland, M. Liu, A. J. Ryan, R. A. L. Jones, S. Huang, and A. Rao, *Nature Materials* **21**, 533 (2022). https://doi.org/10.1038/s41563-022-01204-6

29. R. Pandya, R. Y. S. Chen, Q. Gu, J. Gorman, F. Auras, J. Sung, R. Friend, P. Kukura, C. Schnedermann, and A. Rao, *The Journal of Physical Chemistry A* **124**, 2721 (2020). https://doi.org/10.1021/acs.jpca.0c00346

30. L. Huang, C. Wong, and E. Grumstrup, *J Phys Chem A* **124**, 5997 (2020). https://doi.org/10.1021/acs.jpca.0c05511

31. N. S. Ginsberg, and W. A. Tisdale, *Nature Materials* **21**, 497 (2022). https://doi.org/10.1038/s41563-022-01246-w

32. F. De Martino, G. Valente, N. Staeren, J. Ashburner, R. Goebel, and E. Formisano, *NeuroImage* **43**, 44 (2008). https://doi.org/10.1016/j.neuroimage.2008.06.037

33. M. P. Mcdonald, F. Vietmeyer, D. Aleksiuk, and M. Kuno, *Review of Scientific Instruments* **84**, 113104 (2013). https://doi.org/10.1063/1.4829656

34. M. Welvaert, and Y. Rosseel, *PLoS ONE* **8**, e77089 (2013). https://doi.org/10.1371/journal.pone.0077089

35. M. O'Neill, *ACM Transactions on Mathematical Software*, (2014).

36. C. R. Harris, K. J. Millman, S. J. Van Der Walt, R. Gommers, P. Virtanen, D. Cournapeau, E. Wieser, J. Taylor, S. Berg, N. J. Smith, R. Kern, M. Picus, S. Hoyer, M. H. Van Kerkwijk, M. Brett, A. Haldane, J. F. Del Río, M. Wiebe, P. Peterson, P. Gérard-Marchant, K. Sheppard, T. Reddy, W. Weckesser, H. Abbasi, C. Gohlke, and T. E. Oliphant, *Nature* **585**, 357 (2020). https://doi.org/10.1038/s41586-020-2649-2

37. G. Hodes, and P. V. Kamat, *The Journal of Physical Chemistry Letters* **6**, 4090 (2015). https://doi.org/10.1021/acs.jpclett.5b02052

38. J. More, B. Garbow, and K. Hillstrom, User guide for MINPACK-1. [In FORTRAN], (Office of Scientific and Technical Information (OSTI), 1980), https://doi.org/10.2172/6997568.

39. P. Virtanen, R. Gommers, T. E. Oliphant, M. Haberland, T. Reddy, D. Cournapeau, E. Burovski, P. Peterson, W. Weckesser, J. Bright, S. J. Van Der Walt, M. Brett, J. Wilson, K. J. Millman, N. Mayorov, A. R. J. Nelson, E. Jones, R. Kern, E. Larson, C. J. Carey, İ. Polat, Y. Feng, E. W. Moore, J. Vanderplas, D. Laxalde, J. Perktold, R. Cimrman, I. Henriksen, E. A. Quintero, C. R. Harris, A. M. Archibald, A. H. Ribeiro, F. Pedregosa, P. Van Mulbregt, A. Vijaykumar, A. P. Bardelli, A. Rothberg, A. Hilboll, A. Kloeckner, A. Scopatz, A. Lee, A. Rokem, C. N. Woods, C. Fulton, C. Masson, C. Häggström, C. Fitzgerald, D. A. Nicholson, D. R. Hagen, D. V. Pasechnik, E. Olivetti, E. Martin, E. Wieser, F. Silva, F. Lenders, F. Wilhelm, G. Young, G. A. Price, G.-L. Ingold, G. E. Allen, G. R. Lee, H. Audren, I. Probst, J. P. Dietrich, J. Silterra, J. T. Webber, J. Slavič, J. Nothman, J. Buchner, J. Kulick, J. L. Schönberger, J. V. De Miranda Cardoso, J. Reimer, J. Harrington, J. L. C. Rodríguez, J. Nunez-Iglesias, J. Kuczynski, K. Tritz, M. Thoma, M. Newville, M. Kümmerer, M. Bolingbroke, M. Tartre, M. Pak, N. J. Smith, N. Nowaczyk, N. Shebanov, O. Pavlyk, P. A. Brodtkorb, P. Lee, R. T. Mcgibbon, R. Feldbauer, S. Lewis, S. Tygier, S. Sievert, S. Vigna, S. Peterson, S. More, T. Pudlik, T. Oshima, T. J. Pingel, T. P. Robitaille, T. Spura, T. R.

Jones, T. Cera, T. Leslie, T. Zito, T. Krauss, U. Upadhyay, Y. O. Halchenko, and Y. Vázquez-Baeza, *Nature Methods* **17**, 261 (2020). https://doi.org/10.1038/s41592-019-0686-2

40. W. H. Press, S. A. Teukolsky, W. T. Vetterling, and B. P. Flannery, *Numerical Recipes 3rd Edition: The Art of Scientific Computing* (Cambridge University Press, 2007),

41. P. Roudot, C. Kervrann, F. Waharte, and J. Boulanger, in *2012 19th IEEE International Conference on Image Processing* (IEEE, 2012). https://doi.org/10.1109/icip.2012.6467415

42. N. Tappy, A. Fontcuberta I Morral, and C. Monachon, *Review of Scientific Instruments* **93**, 053702 (2022). https://doi.org/10.1063/5.0080486

43. M. Großmann, S. Bohm, S. Heyder, K. Schwarzburg, P. Kleinschmidt, E. Runge, and T. Hannappel, *physica status solidi (b)* **260**, 2200339 (2023). https://doi.org/10.1002/pssb.202200339

44. A. J. Magdaleno, M. M. Cutler, J. J. Suurmond, M. Meléndez, R. Delgado-Buscalioni, M. Seitz, and F. Prins, *Nanoscale* **15**, 14831 (2023). https://doi.org/10.1039/d3nr03587e

45. J. J. Thiebes, Diffusion Insight Computation Engine (DICE), 1.0.0, (Zenodo, 2023), https://doi.org/10.5281/zenodo.10258191.